



## Research Article

# Performance of Diaphragm Walls during Ultra-Deep Excavations in Karst Areas: Field Monitoring Analysis

Xingzhong Nong,<sup>1</sup> Yanhong Wang,<sup>1</sup> Benhai Lin ,<sup>2,3</sup> Wentian Xu,<sup>1</sup> Wuzhang Luo ,<sup>3,4</sup> and Ren Tang<sup>2,3</sup>

<sup>1</sup>Guangzhou Metro Design & Research Institute Co. Ltd., Guangzhou, China

<sup>2</sup>School of Civil Engineering, Guangzhou University, Guangzhou, China

<sup>3</sup>Guangzhou Geotechnical Investigation & Engineering Design Co. Ltd., Guangzhou, China

<sup>4</sup>Department of Civil and Environmental Engineering, Harbin Institute of Technology, Shenzhen, China

Correspondence should be addressed to Benhai Lin; [linbenhai@gzgeotech.com](mailto:linbenhai@gzgeotech.com) and Wuzhang Luo; [luowuzhang@gzgeotech.com](mailto:luowuzhang@gzgeotech.com)

Received 4 January 2024; Revised 18 March 2024; Accepted 27 March 2024; Published 10 April 2024

Academic Editor: Jianyong Han

Copyright © 2024 Xingzhong Nong et al. This is an open access article distributed under the Creative Commons Attribution License, which permits unrestricted use, distribution, and reproduction in any medium, provided the original work is properly cited.

Deep foundation pit excavations have become more extensive for the construction of underground spaces with rapid urbanization. Diaphragm walls are commonly used to support deep excavations. However, due to the complex geological conditions in karst areas, construction accidents frequently occur during the excavation of foundation pits. This study aims to investigate the performance of diaphragm walls in karst areas through field monitoring analysis. A kick-in deformation mode of the diaphragm wall is revealed during the foundation pit excavation. Furthermore, the results show that the diaphragm walls present multiple deformation modes rather than a single mode. Additionally, this study proposes a method to calculate the lateral displacement of the diaphragm walls at different depths. It is found that the karst caves have a considerable impact on the stability of diaphragm walls, as demonstrated by their lateral displacement. The hidden karst caves reduce the bearing capacity of the bedrock, rendering it insufficient to resist the active earth pressure. As a result, the bottom of the diaphragm wall is kicked into the foundation pit, causing significant lateral displacement and posing risks during excavation. The findings of this study contribute to the design and construction of similar excavations in karst areas.

## 1. Introduction

The rapid development of urbanization has prompted the large-scale construction of underground spaces for high-rise buildings and subway transportation. As a result, deep excavation engineering has become more extensive. The shape of the excavation is typically designed as a rectangle [1–5], circle [6, 7], or irregular polygon [8, 9] based on the superstructure of the buildings and the geological conditions. Construction accidents frequently occur during the excavation of foundation pits, especially in karst areas, due to the complex geological conditions. Therefore, it is crucial to investigate the performance of foundation pits in order to reduce the risk associated with these excavations.

Numerous studies have been conducted to investigate the performance of excavations [10–18]. These studies utilized theoretical analysis, physical model tests, numerical simulations,

and field monitoring. Compared with the other three methods, field monitoring analysis can reflect the realistic stress of the construction sites, and hence, the performance of the excavations can be obtained accurately [19–21]. For instance, Clough and O'Rourke [22] examined the movements of in-situ walls and clarified ground movement patterns by updating the existing database with information from both conventional and new systems. They revealed three typical profiles of movement for braced and tied-back walls. Wang et al. [23] investigated the displacement of retaining walls and the settlements of the ground based on 300 cases of deep excavations in Shanghai soft soils. They found that the ratio of the maximum ground settlement to the maximum lateral displacement of walls ranges from 0.4 to 2.0. Lin et al. [24] proposed a high-risk target model that incorporated the TOPSIS method with hybrid fuzzy sets. They employed a case study of an excavation in Tianjin province, China, to demonstrate the capabilities of the model.

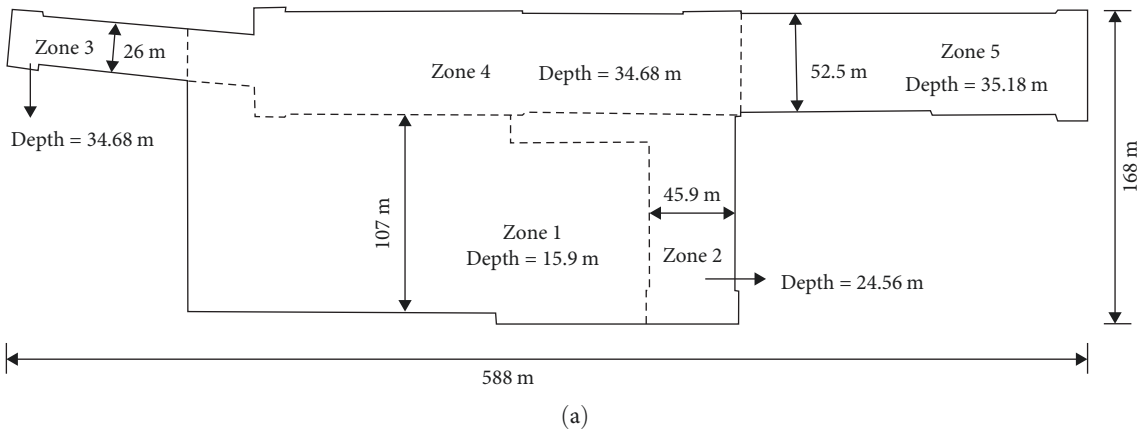


FIGURE 1: Schematic and layout map of the excavation: (a) shape and size of the excavation and (b) layout map of the excavation.

Diaphragm walls, also known as D-walls, are commonly used to provide support for deep excavations due to their high stiffness, strong integrity, and excellent impermeability. The deformation and displacement of diaphragm walls are key parameters that reflect the stability of the excavations. Consequently, extensive investigations have been conducted on the performance of diaphragm walls [25–33]. Karst formations are widely distributed in southern China, including Guangdong, Guangxi, and Hunan. Numerous accidents have occurred during the excavation of foundations due to the presence of karst caves. However, there have been few studies investigating the performance of diaphragm walls in excavations located in karst areas. Karst areas are characterized by the presence of dissolved rock formations, such as limestone, that can create karst caves, potentially leading to instability of supporting structures and ground collapse during deep foundation pit excavation. The impact of karst caves on the stability of diaphragm walls remains unclear.

This study conducted a field monitoring analysis of diaphragm walls in karst areas to assess the performance of D-walls. First, the conditions of the project, including the location and size of the excavation, geological condition, supporting form, and excavation scheme, are presented. Subsequently, the monitoring system for the excavation is described. A method is proposed to calculate the lateral displacement of diaphragm walls by utilizing the deformation

and horizontal movement of the top wall. Lastly, the discussion focuses on the deformation and displacement of diaphragm walls to illustrate the effects of karst caves. The data from this study can assist in calibrating theoretical methods and numerical models. Furthermore, the findings of this study can provide valuable insights for the design and construction of similar foundation pit excavations.

## 2. Project Background

**2.1. Location and Size of the Excavation.** Guangzhou is situated in southern China, specifically in the lower reaches of the Pearl River. The excavation investigated in this study is situated in the northwest of Guangzhou, near the Shijin River.

As depicted in Figure 1, the excavation was designed in the shape of an irregular polygon. The excavation has a length of 588 m and a width of 168 m. The irregular shape and large size of the excavation heighten the risk associated with the foundation pit excavation. In order to induce the risk of excavation, the foundation pit was divided into five zones (i.e., Zone 1–Zone 5 in Figure 1(a)). The width of each zone is provided in Figure 1. The depths of Zone 1 and Zone 2 are 15.9 and 24.56 m, respectively. Both of the depths of Zone 3 and Zone 4 are 34.68 m. The depth of Zone 5 is 35.18 m.

**2.2. Geological Condition in Karst Area.** The geological profiles of these five zones are depicted in Figure 2. The subsoils comprise fill, muddy clay, medium-coarse sand, and silty clay. Calcareous shale and limestone are underlying the soil layers. The thickness of soils and rocks varies significantly among different excavation zones. Table 1 displays the soil properties, including natural density, water content, void ratio, cohesion, friction angle, coefficient of compressibility, modulus of compressibility, and deformation modulus. Table 2 presents the properties of the calcareous shale and limestone, including the coefficient of compressibility, modulus of compressibility, deformation modulus, and standard value of uniaxial ultimate compressive strength.

Limestone belongs to soluble carbonate rocks that are easily dissolved by the rapid downward movement of groundwater. Subsequently, karst caves are formed within the limestone layer, as depicted in Figure 3. Based on the geology profiles, limestone is widely distributed throughout the excavation site. Furthermore, Guangzhou experiences abundant rainfall, resulting in a high water table. Consequently, karst caves are extensively formed within the excavation site, as shown in Figure 2, thereby increasing the risk associated with the excavation.

**2.3. Construction Phases and Retaining Structures.** The construction phases of the excavation are presented in Tables 3 and 4. The excavation of the foundation pit lasts approximately 2 years, from June 12th, 2020, to May 8th, 2022. It should be noted that March 26th, 2019, the commencement date of the excavation monitoring, is designated as day 0 in this study for the purpose of presenting the results conveniently and succinctly in the subsequent sections.

Figure 2 displays the schematic cross-section views of the excavation's retaining structures. The first struts of Zone 1–Zone 4 are located at a depth of 5.0 m, while the first strut of Zone 5 is located at a depth of 1.3 m. The second struts of Zone 1–Zone 4 are located at a depth of 10.0 m, while the strut of Zone 5 is at a depth of 6.85 m. The third struts of Zone 2–Zone 4 are located at a depth of 16.5 m, while the third struts of Zone 5 are at a depth of 13.15 m. The fourth struts of Zone 3–Zone 5 are located at a depth of 20.45 m. The last struts of Zone 4 and Zone 5 are located at a depth of 26.45 m.

### 3. Methodology of Monitoring

**3.1. Monitoring Equipment.** The horizontal displacement at the top of the D-walls was measured using a TS16 electronic total station with a precision of  $\pm 1.0$  mm. A positive displacement indicates movement toward the excavation, while a negative displacement indicates movement away from the excavation. The deformation of the D-walls was measured using SINCO50302510 clinometers with a precision of 0.02 mm per 500 mm. The location of the monitoring points is illustrated in Figure 4.

This paper presents the theory of clinometer measurement to propose a method for calculating the lateral

displacement of D-walls. As depicted in Figure 5(a), guide casing is pre-embedded in the diaphragm wall. When measuring the deformation of the D-walls, the inclinometer probe is inserted at the bottom of the D-walls and then lifted upward. The inclination angle ( $\theta_i$ ,  $i = 1, 2, \dots, n$ ) of the D-walls can be measured successively (as shown in Figure 5). The deformation of the D-walls at each depth ( $\Delta s_i$ ) can be calculated using the following equation:

$$\Delta s_i = \sum L \sin \theta_i, \quad (1)$$

where  $L$  is the distance between successive readings. It should be noted that the calculation of deformation assumes that the bottom of the D-walls is fixed.

**3.2. Method to Calculate the Lateral Displacement of the D-Walls.** The deformation of the D-walls is equal to the lateral displacement only when the bottom of the D-walls is fixed. However, if there are unknown karst caves in the foundation pit, the bearing capacity of the D-walls may not be sufficient to withstand the active earth pressure. Consequently, the bottom of the D-walls may be pushed inward during the excavation of the foundation pit. The lateral displacement of the D-walls will not be equal to the deformation. Therefore, a method is proposed to calculate the lateral displacement of the D-walls.

Figure 6 illustrates the six statuses of the deformed D-walls based on the position of their top and bottom, encompassing all possible scenarios. In cases (A) and (B), both the top and bottom of the D-walls move toward the foundation pit. In case (A), the top of the D-walls is positioned on the right side of the vertical line, while in case (B), it is located on the left side of the vertical line. In case (A), the top of the D-walls is positioned on the right side of the vertical line, while in case (B), it is located on the left side of the vertical line. In case (A), the top of the D-walls is positioned on the right side of the vertical line, while in case (B), it is located on the left side of the vertical line. In contrast to case (E), the bottom of the D-walls moves away from the foundation pit, while the top of the D-walls moves toward the foundation pit in case (F).

The lateral displacement of the bottom of the diaphragm walls ( $\delta_b$ ) can be calculated by utilizing the horizontal displacement and the deformation at the top of the D-walls, as follows:

$$\delta_b = \delta_t - \Delta s, \quad (2)$$

where  $\delta_t$  is the horizontal displacement at top of the D-walls,  $\Delta s$  is the deformation at top of the D-walls. If  $\delta_b$  is equal to zero (i.e.,  $\delta_t = \Delta s$ ), it means that the bottom of the D-walls is stable.  $\delta_t^{(+)}$  represents the top of the D-walls moves toward the foundation pit, whereas  $\delta_t^{(-)}$  represents the top of the D-walls moves away from the foundation pit.  $\Delta s^{(+)}$  represents the top of the D-walls is on the right side of the vertical

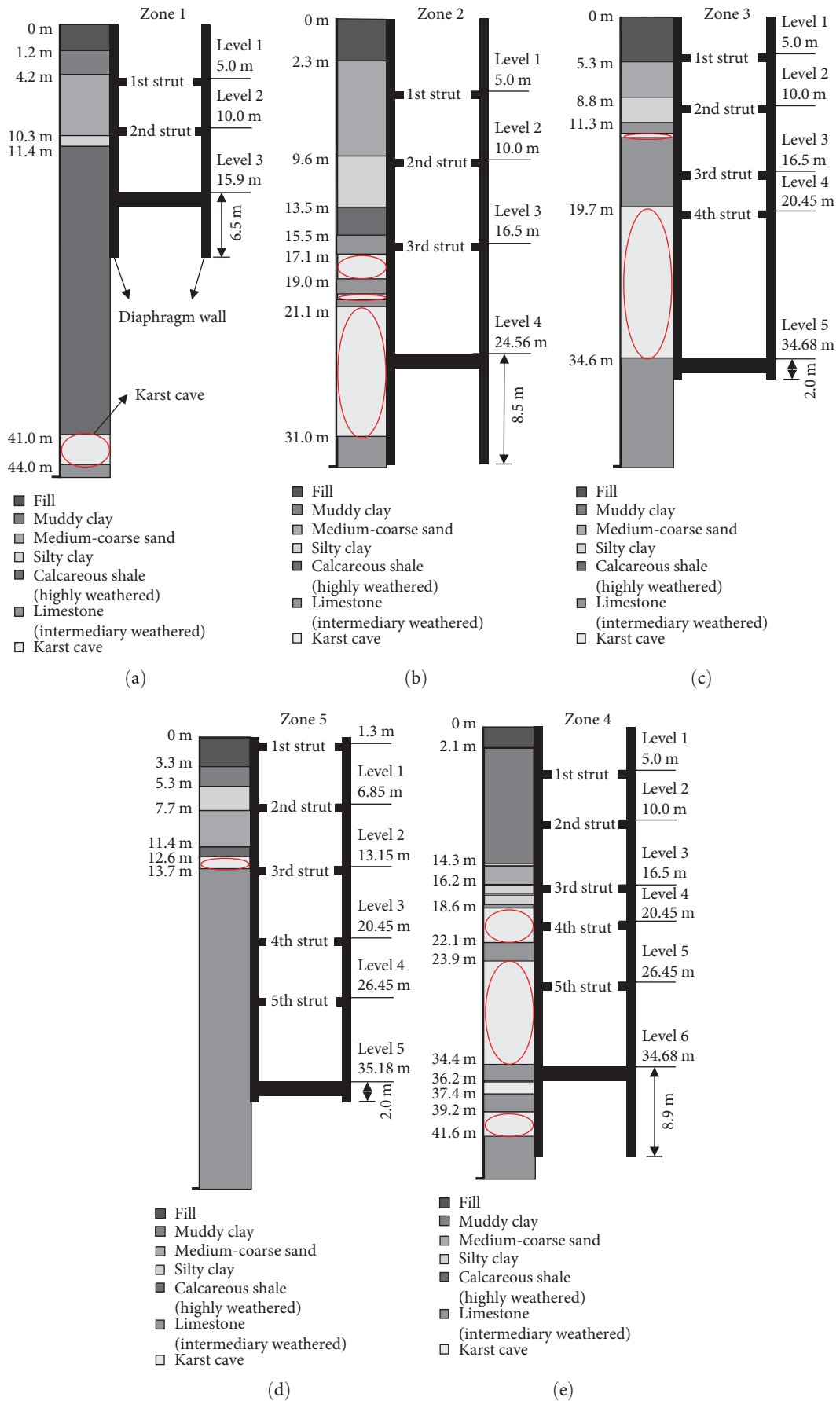


FIGURE 2: Geological profile of the excavation site: (a) Zone 1, (b) Zone 2, (c) Zone 3, (d) Zone 4, and (e) Zone 5.

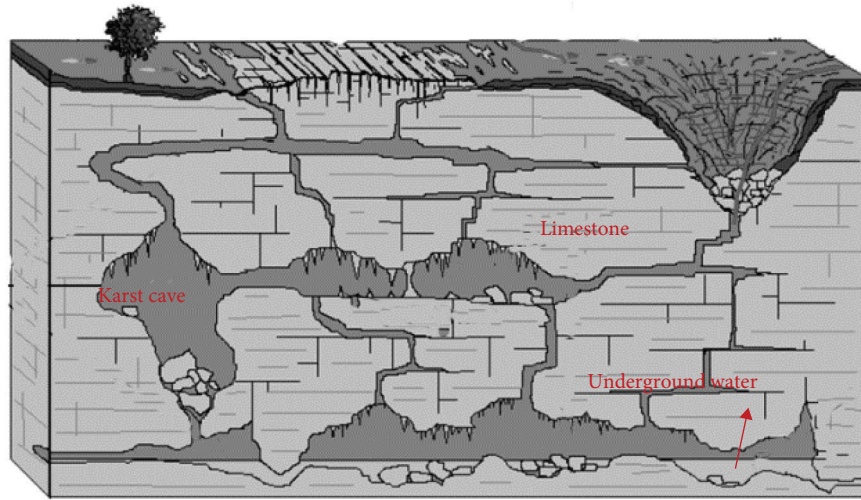


TABLE 1: Soil properties of clay and sand in the excavation site.

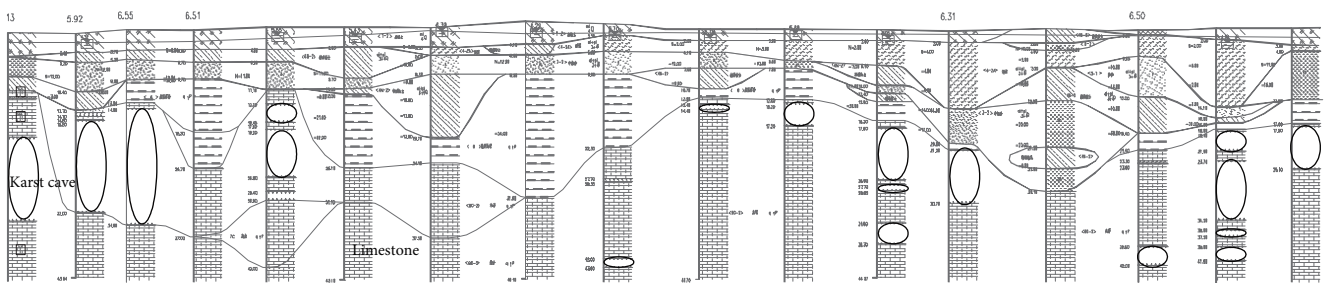
Soils	Density (g/cm <sup>3</sup> )	Water content (%)	Void ratio	Cohesion (kPa)	Friction angle (°)	Coefficient of compressibility (MPa <sup>-1</sup> )	Modulus of compressibility (MPa)	Deformation modulus (MPa)
Fill	1.90	28.80	0.810	19.40	6.80	0.40	4.50	10.0
Muddy clay	1.57	67.20	1.860	6.21	2.97	1.63	1.97	3.0
Silty clay	1.88	28.94	0.840	21.58	9.44	0.44	4.51	10.0
Sand	1.90	—	0.700	0	30.00	—	9.50	12.0

TABLE 2: Properties of rock in the excavation site.

Rock	Coefficient of compressibility (MPa <sup>-1</sup> )	Modulus of compressibility (MPa)	Deformation modulus (MPa)	Standard value of uniaxial ultimate compressive strength (MPa)
Calcareous shale	0.20	33.00	127.00	9.00
Limestone	—	50.00	—	26.35



(a)



(b)

FIGURE 3: Karst caves: (a) schematic of karst caves and (b) geological structure profiles.

line whereas  $\Delta s^{(-)}$  represents the top of the D-walls is on the left side of the vertical line.

The horizontal displacement at different depths of the D-walls ( $\delta_i$ ) can be calculated by utilizing the lateral displacement at the bottom of the D-walls and the deformation at the corresponding depth ( $\Delta s_i$ ), as follows:

$$\delta_i = \delta_b + \Delta s_i. \tag{3}$$

## 4. Results and Discussion

4.1. Horizontal Displacement at the Top of D-Walls. Figure 7 illustrates the horizontal displacement at the top of the

TABLE 3: Schedule of construction phases of Zone 1–Zone 3.

Zones	Description	Start date (day from 2019/3/26)	End date (day from 2019/3/26)	Stage
Zone 1	Excavate to Level 1 (−5.0 m)	2020/06/12 (Day 444)	2020/07/02 (Day 464)	Stage 1
	Construct 1st strut	2020/07/07 (Day 469)	2021/01/09 (Day 655)	Stage 2
	Excavate to Level 2 (−10.0 m)	2021/01/15 (Day 661)	2021/03/16 (Day 721)	Stage 3
	Construct 2nd strut	2021/03/24 (Day 729)	2021/04/10 (Day 746)	Stage 4
	Excavate to Level 3 (−15.9 m)	2021/04/13 (Day 749)	2021/06/30 (Day 827)	Stage 5
	Finish the base plate	2021/07/01 (Day 828)	2022/05/08 (Day 1,139)	Stage 6
Zone 2	Excavate to Level 1 (−5.0 m)	2020/06/12 (Day 444)	2020/07/02 (Day 464)	Stage 1
	Construct 1st strut	2020/07/07 (Day 469)	2021/01/09 (Day 655)	Stage 2
	Excavate to Level 2 (−10.0 m)	2021/01/21 (Day 667)	2021/02/26 (Day 703)	Stage 3
	Construct 2nd strut	2021/02/28 (Day 705)	2021/03/19 (Day 724)	Stage 4
	Excavate to Level 3 (−16.5 m)	2021/03/28 (Day 733)	2021/04/13 (Day 749)	Stage 5
	Construct 3rd strut	2021/04/20 (Day 756)	2021/07/15 (Day 842)	Stage 6
	Excavate to Level 4 (−24.56 m)	2021/07/24 (Day 851)	2022/02/11 (Day 1,053)	Stage 7
Zone 3	Excavate to Level 1 (−5.0 m)	2020/06/12 (Day 444)	2020/07/02 (Day 464)	Stage 1
	Construct 1st strut	2020/07/07 (Day 469)	2020/11/20 (Day 605)	Stage 2
	Excavate to Level 2 (−10.0 m)	2020/12/04 (Day 619)	2020/12/09 (Day 624)	Stage 3
	Construct 2nd strut	2020/12/10 (Day 625)	2020/12/18 (Day 633)	Stage 4
	Excavate to Level 3 (−16.5 m)	2020/12/20 (Day 635)	2021/01/10 (Day 656)	Stage 5
	Construct 3rd strut	2021/01/13 (Day 659)	2021/02/02 (Day 679)	Stage 6
	Excavate to Level 4 (−20.45 m)	2021/03/16 (Day 721)	2021/04/22 (Day 758)	Stage 7
	Construct 4th strut	2021/07/18 (Day 845)	2021/09/02 (Day 891)	Stage 8
	Excavate to Level 5 (−34.68 m)	2021/11/01 (Day 951)	2022/05/08 (Day 1,139)	Stage 9

TABLE 4: Schedule of construction phases of Zone 4 and Zone 5.

Zones	Description	Start date (day from 2019/3/26)	End date (day from 2019/3/26)
Zone 4	Excavate to Level 1 (−5.0 m)	2020/06/12 (Day 444)	2020/07/02 (Day 464)
	Construct 1st strut	2020/07/07 (Day 469)	2020/08/31 (Day 524)
	Excavate to Level 2 (−10.0 m)	2020/09/25 (Day 549)	2020/10/30 (Day 584)
	Construct 2nd strut	2020/11/12 (Day 597)	2021/02/06 (Day 683)
	Excavate to Level 3 (−16.5 m)	2021/02/20 (Day 697)	2021/04/05 (Day 741)
	Construct 3rd strut	2021/04/13 (Day 749)	2021/06/16 (Day 813)
	Excavate to Level 4 (−20.45 m)	2021/07/12 (Day 839)	2021/07/21 (Day 848)
	Construct 4th strut	2021/07/24 (Day 851)	2021/08/15 (Day 873)
	Excavate to Level 5 (−26.45 m)	2021/08/24 (Day 882)	2021/09/16 (Day 905)
	Construct 5th strut	2021/09/21 (Day 910)	2021/12/06 (Day 986)
	Excavate to Level 6 (−34.68 m)	2021/12/29 (Day 1,009)	2022/05/08 (Day 1,139)
	Construct 1st strut	2020/07/07 (Day 469)	2020/07/15 (Day 477)
	Excavate to Level 1 (−6.85 m)	2020/07/22 (Day 484)	2020/07/28 (Day 490)
	Construct 2nd strut	2020/08/04 (Day 497)	2020/10/05 (Day 559)
Zone 5	Excavate to Level 2 (−13.15 m)	2020/10/13 (Day 567)	2020/10/27 (Day 581)
	Construct 3rd strut	2020/11/12 (Day 597)	2020/12/04 (Day 619)
	Excavate to Level 3 (−20.45 m)	2020/12/14 (Day 629)	2021/01/02 (Day 648)
	Construct 4th strut	2021/01/05 (Day 651)	2021/02/03 (Day 680)
	Excavate to Level 4 (−26.45 m)	2021/02/12 (Day 689)	2021/04/05 (Day 741)
	Construct 5th strut	2021/04/13 (Day 749)	2021/05/09 (Day 775)
	Excavate to Level 5 (−35.18 m)	2021/05/17 (Day 783)	2021/07/26 (Day 853)

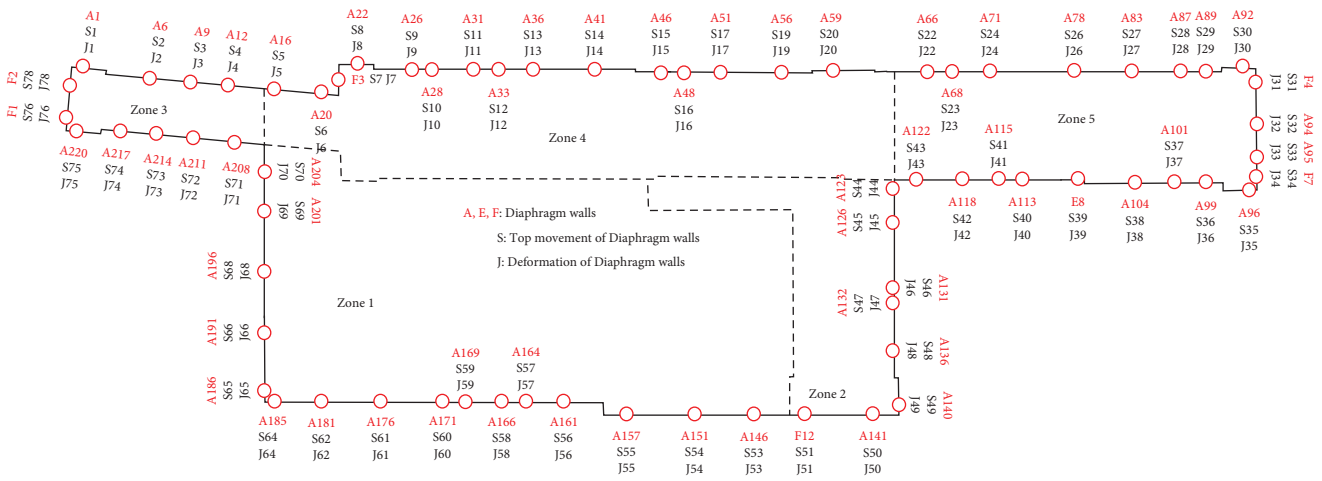


FIGURE 4: Monitoring scheme.

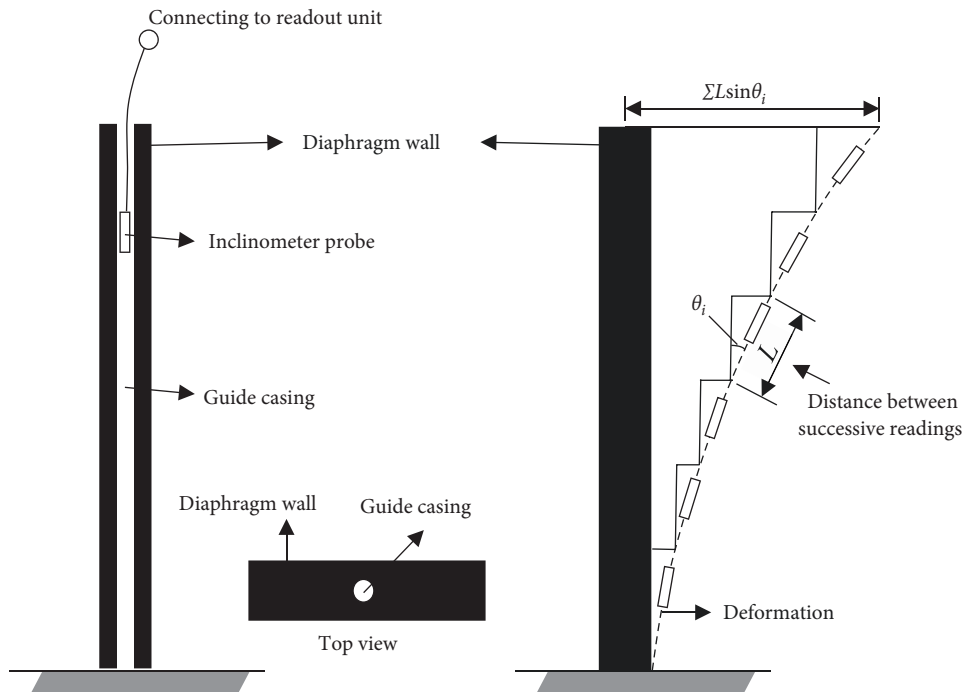


FIGURE 5: Theory of the inclinometer.

diaphragm walls (note that only representative results are shown). In Figure 7(a), the horizontal displacement of the D-walls in Zone 1 gradually increases during the excavation of the foundation pit. At day 950, the horizontal displacement of A181 (monitored at point S62) and A191 (monitored at point S66) experienced a sharp increase as the struts were removed. The displacement reached its maximum values within approximately 10 days (51.6 mm for A181 and 33.0 mm for A191). The removal of struts is a construction process associated with high risk. Therefore, timely replacement of supports is crucial for mitigating construction risks.

As depicted in Figure 7(b), the horizontal displacement of A123 (monitored at point S44) in the external corner of

the foundation pit rapidly increased and reached its maximum value of 19.0 mm during excavation. In contrast, the horizontal displacement of A140 (monitored at point S49) in the internal corner of the foundation pit was minimal, with a maximum value of only -1.5 mm. This is because the D-walls experience higher pressure in the external corner compared to the internal corner.

Figure 7(c) illustrates that the top of the majority of D-walls in Zone 3 exhibited movement away from the foundation pit during excavation, which contradicted the findings of Wang et al. [34]. The top horizontal movement of A9 (monitored at point S3), A16 (monitored at point S5), and A211 (monitored at point S72) exhibited rapid increases following the completion of the final level excavation. To

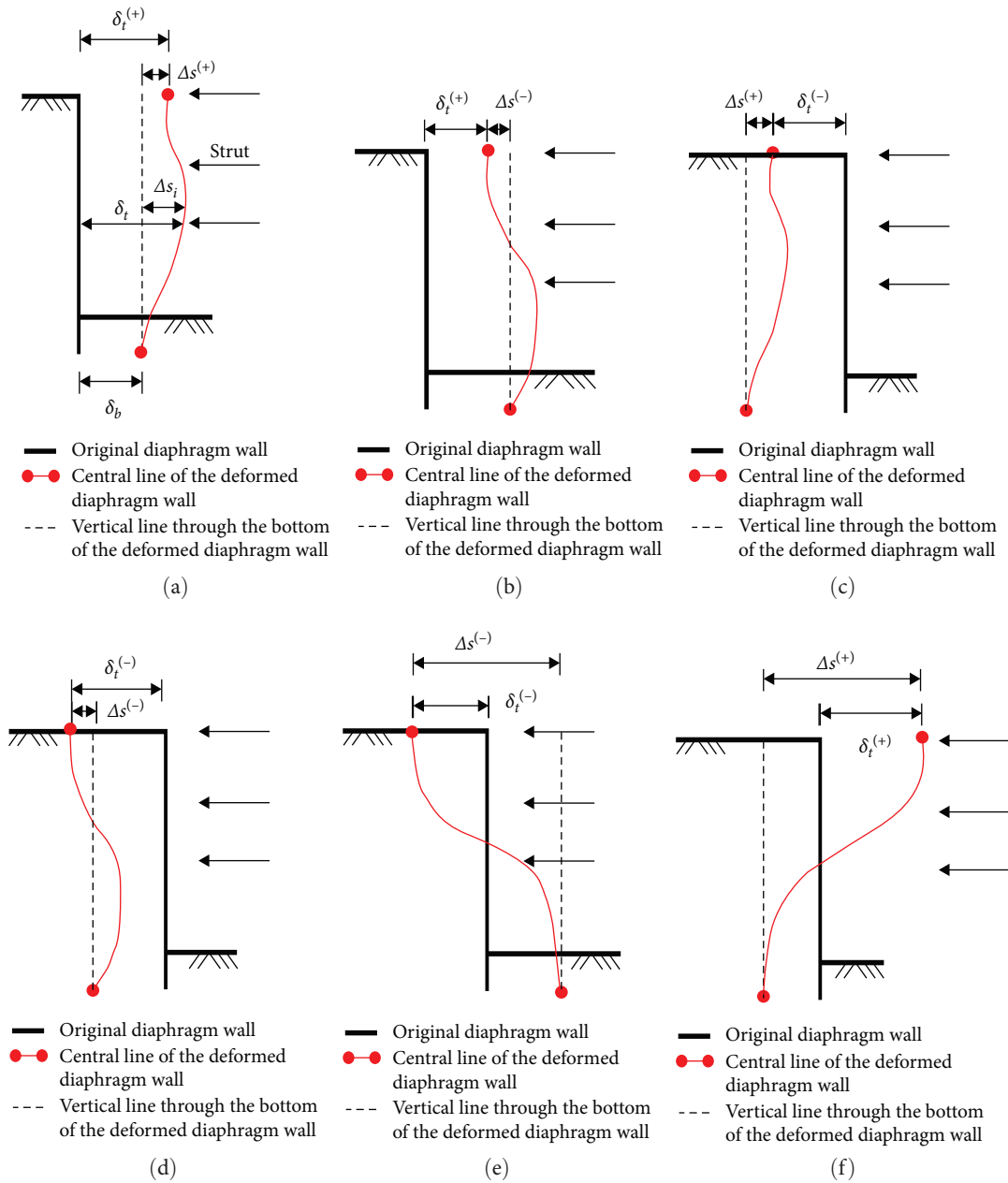


FIGURE 6: Schematics of the deformation and the displacement of the diaphragm walls: (a) Case A, (b) Case B, (c) Case C, (d) Case D, (e) Case E and (f) Case F.

investigate the cause, several boreholes were conducted in Zone 3. Consequently, the bearing capacity of the bedrock proved inadequate in resisting the active earth pressure at the bottom of the D-walls. The lower portion of the D-walls experienced inward movement within the foundation pit, as depicted in Figure 6(e). A similar phenomenon was observed in A20 (monitored at point S6) in Zone 4, as demonstrated in Figure 7(d).

Figure 7(e) illustrates the horizontal displacement at the top of D-walls in Zone 5. The displacement in Zone 5 was comparatively smaller, and the D-walls exhibited greater stability than that observed in the D-walls of other zones. This is attributed to the limited presence of karst caves in the bedrock of Zone 5, which provides sufficient bearing capacity to

withstand the earth's pressure. The displacement of A104 (monitored at point S38) and A122 (monitored at point S43) increased between day 567 and day 657 due to the substantial construction load. Following the removal of the construction load, the horizontal displacement of the diaphragm walls decreased.

4.2. Deformation of the D-Walls. The identification of distinct deformation modes of the D-walls during excavation is crucial for design purposes. Clough and O'Rourke [22] observed three distinct deformation modes in the in-situ walls, as depicted in Figure 8. It is evident that the walls deformed toward the foundation pit in all modes as a result of the active earth pressure. Figure 9 illustrates the deformation of the



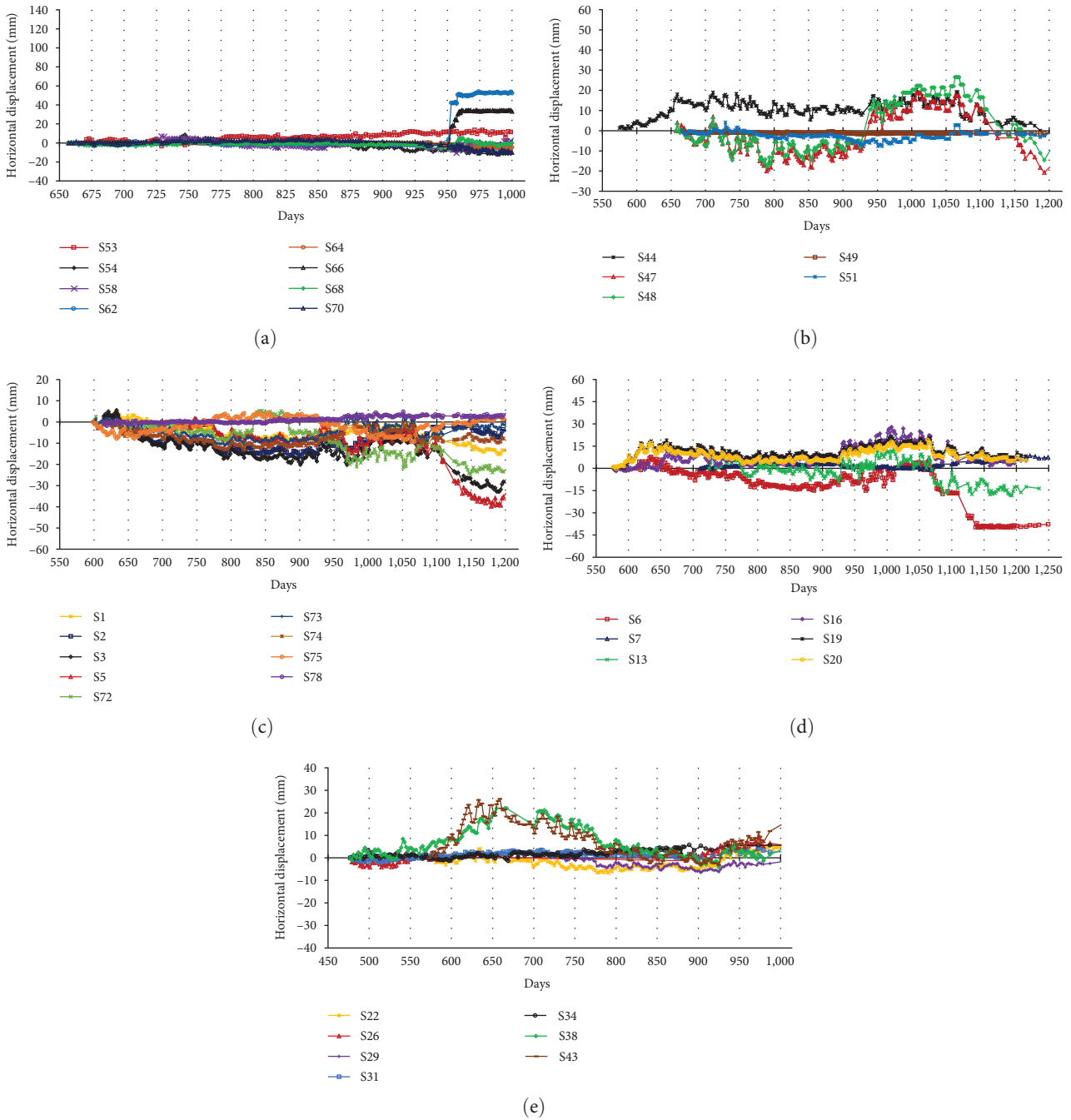


FIGURE 7: Horizontal displacement at the top of diaphragm walls in (a) Zone 1, (b) Zone 2, (c) Zone 3, (d) Zone 4, and (e) Zone 5.

representative D-walls during the excavation of the foundation pit in this study. Multiple deformation modes can be observed within the same D-walls during excavation, which differs from the single parabolic deformation mode reported by Wang et al. [34] in soft ground. Furthermore, an unexpected deformation mode can be observed, as depicted in Figure 10. The lower portion of the D-wall deforms toward the excavation, while the upper portion deforms toward the outside of the foundation pit. For instance, A146 (monitored at J53) and A157 (monitored at J55) exhibited this deformation mode. This deformation mode is referred to as the kick-in mode in this study.

To provide a clear observation of the D-wall deformation process during excavation, examples are illustrated in Figure 11. Figure 11(a) illustrates the deformation process of D-wall A146 (monitored at J53) during the excavation of the foundation pit. The deformation of A146 remained minimal after the foundation pit was excavated to Level 2 (at Stage 1). Upon excavating the foundation pit to Level 3 (at Stage 3), the deformation increased, with a maximum deformation of  $-16.2$  mm observed at the top of A146. After a period of 312 days (at Stage 6), the construction of the base plate for the foundation pit was finalized, and the kick-in deformation mode was observed. The deformation at the top of A146 increased to

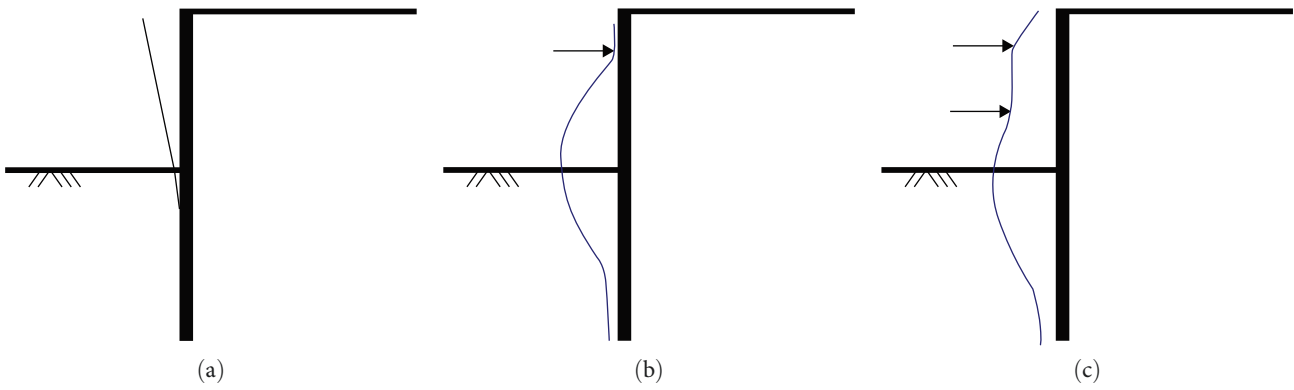


FIGURE 8: Typical deformation modes of D-walls found by Clough and O'Rourke: (a) cantilever mode, (b) parabolic mode, and (c) combined mode.

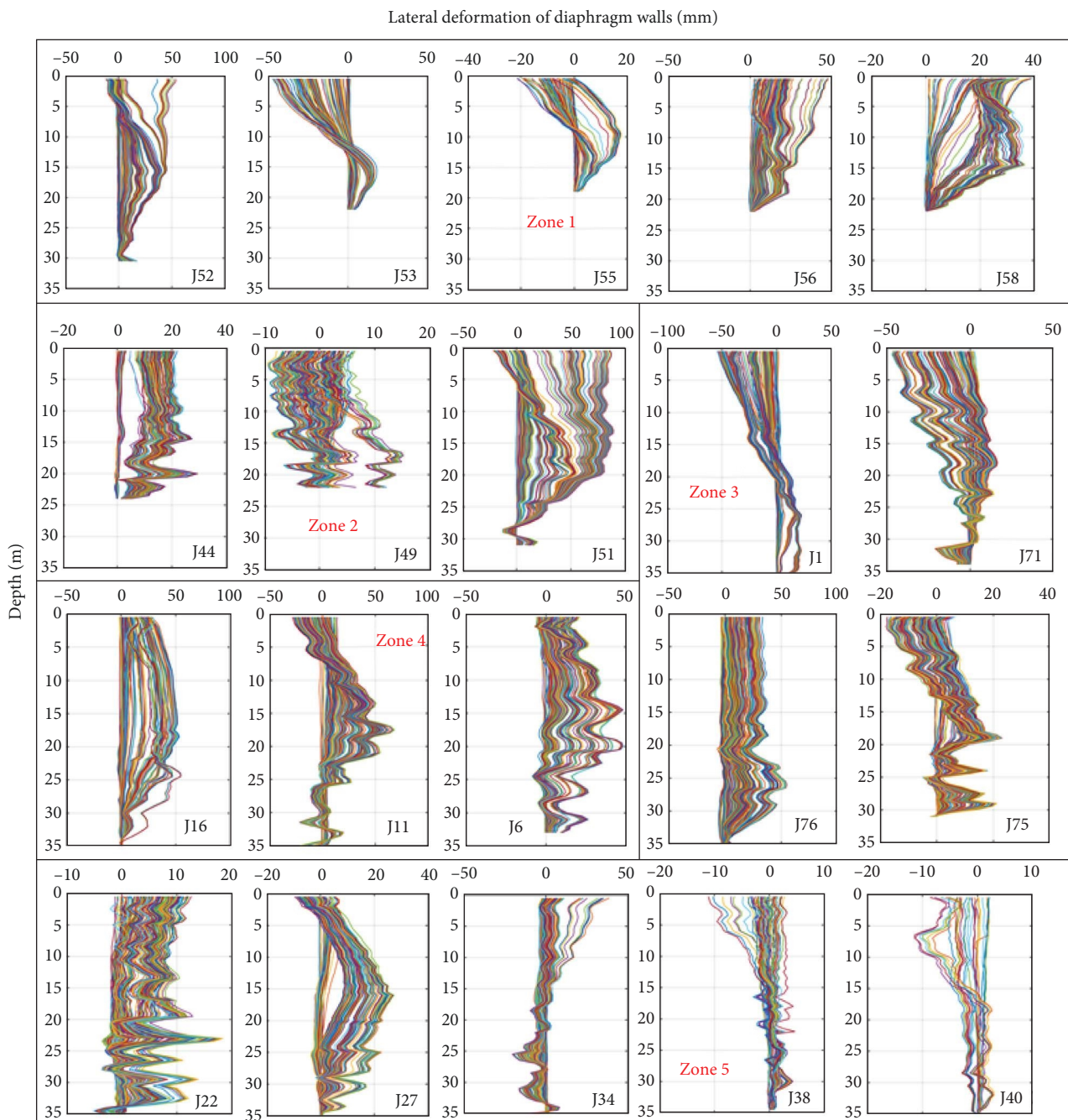


FIGURE 9: Lateral deformation of the diaphragm walls during the excavation.

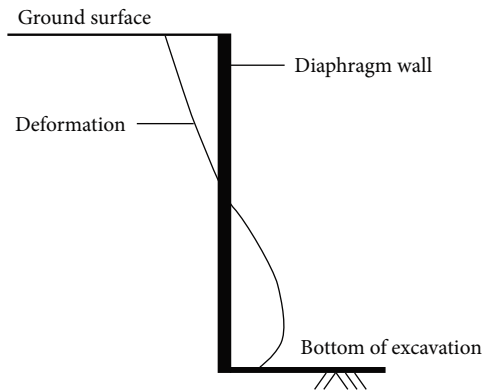


FIGURE 10: Kick-in deformation mode of D-walls found in Karst areas.

−26.2 mm, while the lower portion of the D-walls deformed toward the foundation pit, reaching a maximum deformation of 15.9 mm at a depth of 16.5 m below the bottom of the foundation pit.

The deformation process of D-wall A166 (monitored at J58) is illustrated in Figure 11(b). Following the completion of Level 1 excavation (at Stage 1), A166 exhibited minimal deformation. Upon completion of the Level 2 excavation (at Stage 2), A166 displayed cantilever deformation. The maximum deformation, located at the top of A166, reached 32.5 mm. Upon completion of the first strut, the maximum deformation decreased to 27.3 mm. After a period of 312 days, the parabolic deformation mode was observed. The maximum deformation, at a depth of 14.5 m, reached 33.4 mm.

The deformation process of D-wall A181 (monitored at J62) is illustrated in Figure 11(c). The cantilever deformation mode was observed at both Stage 1 and Stage 3. Upon completion of the first and second struts, the cantilever deformation mode transitioned to the parabolic deformation mode at Stage 5. A181 experienced a maximum deformation of 20.3 mm at a depth of 13 m. Upon removal of the angle strut, the parabolic deformation mode reverted back to the cantilever deformation mode. The deformation of the D-wall rapidly increased. At Stage 6, A181 experienced a significant maximum deformation of 64.5 mm, resulting in the development of cracks.

The deformation process of A1 in Zone 3 is depicted in Figure 11(d). The deformation process of A1 exhibited similarities to that of A146. A maximum deformation of −40.5 mm was recorded at Stage 5. Upon completion of the third strut and excavation of the foundation pit to Level 4 (at Stage 7), the maximum deformation of A1 decreased to −5.6 mm. However, upon excavation of the foundation pit to Level 5, the deformation mode transitioned to the kick-in deformation mode, resulting in increased deformation. The deformation at the top of A1 escalated to −33.9 mm. The lower portion of the D-walls deformed toward the foundation pit, with a maximum deformation of 21.4 mm at a depth of 26 m.

In summary, the excavation of foundation pits in karst areas reveals four distinct deformation modes of D-walls. Prior to the construction of any struts, the D-walls

exhibit a cantilever mode during excavation, as depicted in Figure 8(a). Once the first strut is constructed, the D-walls exhibit a parabolic mode due to the constraint at the top, resulting in minimal deformation (Figure 8(b)). As the excavation depth increases and additional struts are constructed, the D-walls transition into a combined mode characterized by increased deformation and deformation toward the foundation pit (Figure 8(c)). In the presence of hidden karst caves within the foundation pit and the absence of any surcharge along its edges, the deformation mode of the D-wall exhibits the kick-in deformation mode (Figure 10). During the excavation process, if monitoring data indicate the kick-in deformation mode of D-walls, it is likely that hidden karst caves are present in close proximity to the D-walls. Boreholes should be conducted to identify the presence of karst caves, and appropriate treatment measures should be implemented to mitigate significant displacement of the D-walls and ensure safe excavation.

**4.3. Lateral Displacement of the D-Walls.** As mentioned in previous sections, the lateral displacement of the D-walls is equivalent to the lateral deformation, but only when the bottom of the D-walls is fully constrained, resulting in zero displacement. However, the bottom of the D-walls frequently shifted toward the foundation pit due to the presence of unknown karst caves in karst areas. Therefore, the lateral displacement at the bottom of the D-walls should be computed using Equation (2), while the lateral displacement at different depths of the D-walls should be calculated using Equation (3).

Figure 12 illustrates the variations in the lateral displacement of representative D-walls (A146, A166, A181, and A1) throughout the excavation of the foundation pit. Figure 12(a) displays the lateral displacement of A146. It is evident that the D-wall uniformly shifted toward the foundation pit due to the active earth pressure. At Stage 3, the maximum displacement, located at a depth of 10.0 m, was recorded at 6.3 mm. Following the completion of Level 3 excavation, the displacement at the lower position of the D-wall exhibited a rapid increase, with a maximum displacement of 23.6 mm at a depth of 16.0 m. Additional boreholes were conducted near A146 in the foundation pit to investigate the cause of this response. Unexpected karst caves were observed (as depicted in Figure 13(a)). The active earth pressure compressed and caused the collapse of the karst caves, thereby reducing the bearing capacity of the bedrock and resulting in a rapid increase in displacement at the lower position of the D-wall. After a period of 312 days (at Stage 6), the maximum displacement increased to 62.9 mm at a depth of 17.0 m. The D-walls uniformly shift toward the foundation pit under the active earth pressure and surcharge. The presence of unknown karst caves results in a larger displacement at the lower position of the D-walls compared to the upper position. In this study, this behavior exhibited by the D-walls is classified as a Type A response, as depicted in Figure 13(b).

Figure 12(b) illustrates the lateral displacement of A166 throughout the excavation of the foundation pit. The displacement of A166 closely aligned with the deformation of

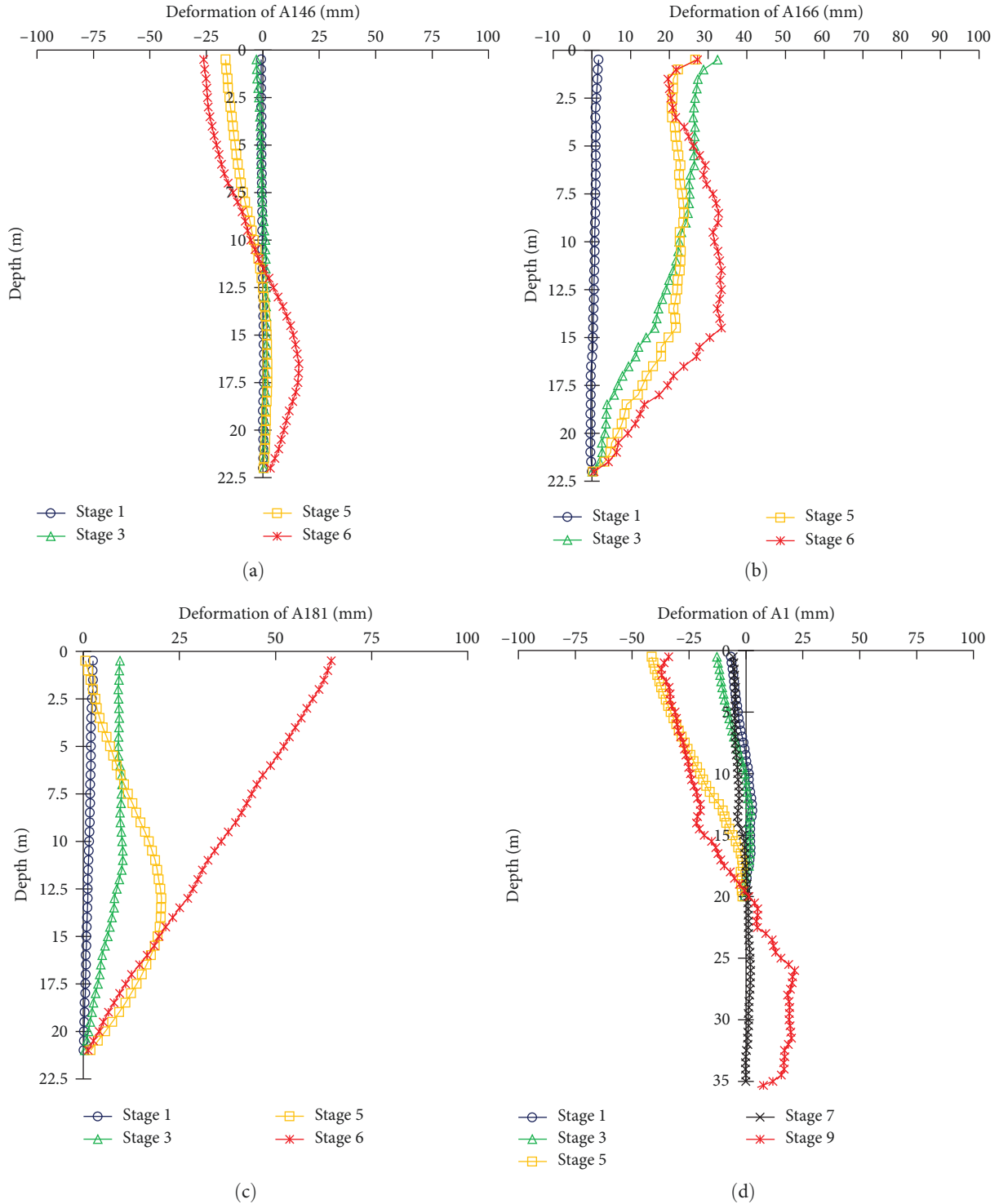


FIGURE 11: Deformation of D-walls during foundation pit excavation: (a) A146 of Zone 1, (b) A166 of Zone 1, (c) A181 of Zone 1, and (d) A1 of Zone 3.

A166 (as depicted in Figure 11(b)) due to the complete fixation of its bottom in the bedrock. Following the completion of Level 1 excavation at Stage 1, A166 exhibited a maximum displacement of merely 1.7 mm. The displacement of the D-wall increased as the foundation pit excavation progressed. At Stage 5, the maximum displacement of the D-walls

reached 22.9 mm at a depth of 8.5 m. After a period of 312 days (at Stage 6), the maximum displacement of the D-walls measured 33.1 mm at a depth of 14.5 m.

Figure 12(c) illustrates the lateral displacement of A181 throughout the excavation of the foundation pit. The displacement of the D-wall was relatively negligible when the

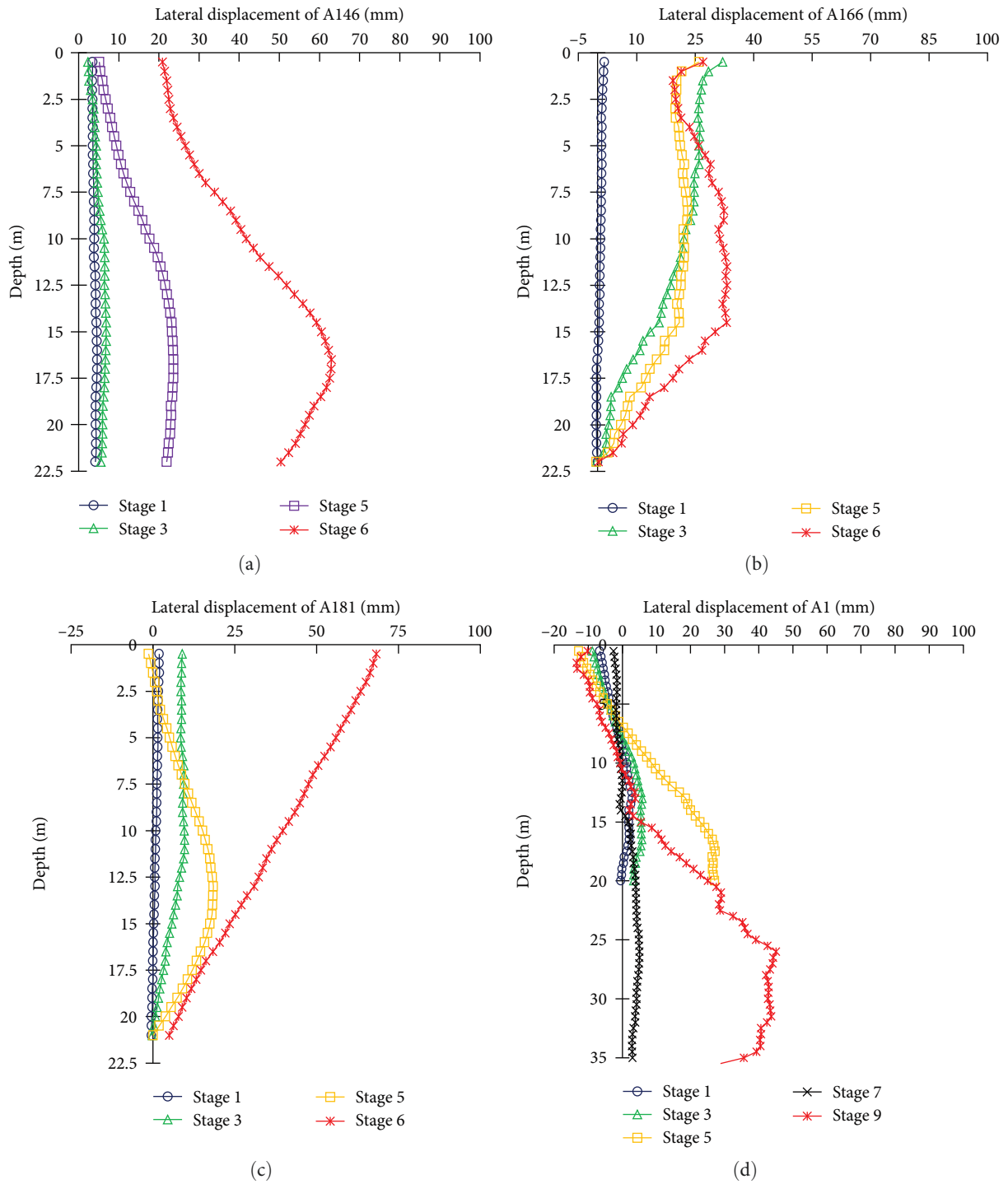


FIGURE 12: Lateral displacement of D-walls during foundation pit excavation: (a) A146 of Zone 1, (b) A166 of Zone 1, (c) A181 of Zone 1, and (d) A1 of Zone 3.

foundation pit was excavated to  $-5.0$  m. Once the foundation pit reached a depth of  $10.0$  m, the maximum displacement, occurring at the top of A181, measured  $9.0$  mm. Upon completion of the final-level excavation, the maximum displacement increased to  $18.3$  mm, situated at a depth of  $14.0$  m. After the removal of the struts, the displacement rapidly increased. At Stage 6, the maximum displacement peaked at  $68.3$  mm, located at the top of D-wall A181.

Figure 12(d) illustrates the lateral displacement of A1 throughout the excavation of the foundation pit. It is observed that the top of the D-wall shifted outward from the foundation pit after the completion of the first level excavation at a depth of  $-5.0$  m. The D-wall started to tilt. As the foundation excavation progressed, the angle of inclination of the D-wall continued to increase. This is attributed to the presence of karst caves in the foundation pit, as depicted in



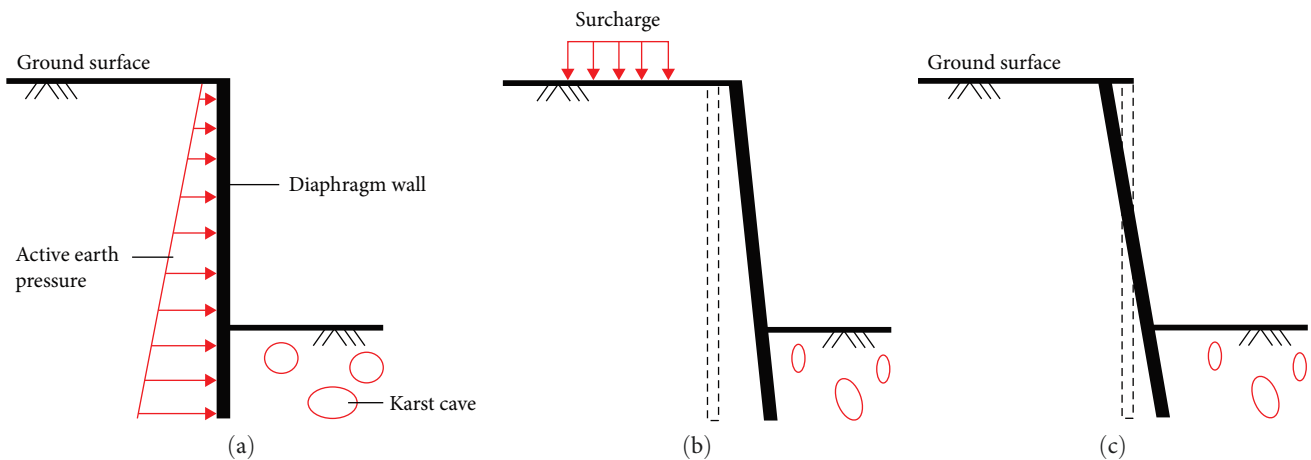


FIGURE 13: Schematics of D-walls responses in foundation pit with unknown karst caves: (a) foundation pit with unknown karst caves, (b) Type 1 response, and (c) Type 2 response.

Figure 13(c). The presence of karst caves diminished the bearing capacity of the bedrock, rendering it incapable of withstanding the active earth pressure at the bottom of the D-walls. Consequently, the bottom of the D-walls experienced inward movement within the foundation pit, causing the top of the D-walls to shift outward without any external load. This behavior of the D-walls is classified as a Type B response in this study. The completion of the third strut resulted in a reduction in the displacement of the D-walls. Upon the completion of the fourth level excavation, the D-wall exhibited a maximum displacement of 5.0 mm. Subsequent to the completion of the final level excavation, the displacement of the D-wall once again experienced an increase. This was attributed to the excessive excavation depth between Level 4 and Level 5, which reached 14.23 m. The bearing capacity of the bedrock proved inadequate in withstanding the active earth pressure.

## 5. Summary and Conclusions

This study investigates the performance of diaphragm walls during the excavation of ultra-deep foundation pits in karst areas through field monitoring analysis. The horizontal movement at the top and the deformation of the diaphragm walls were monitored. The proposed method enables accurate calculation of the lateral displacement of the diaphragm walls at different depths. The study yields the following conclusions:

- (1) In addition to the three typical deformation modes (i.e., cantilever model, parabolic mode, and combined mode), this study identifies a new kick-in deformation mode of the diaphragm walls in the karst area. Furthermore, during the excavation of deep foundation pits, the diaphragm walls exhibit multiple deformation modes instead of a singular mode.
- (2) The embedded depth of diaphragm walls should be increased during the design of the excavation to prevent kick-in failure in the karst area. During the construction of the excavation, if the kick-in deformation

mode is observed in the monitoring data, borehole drillings should be conducted to identify hidden karst caves. Subsequently, appropriate treatment measures should be implemented to mitigate significant displacement of the diaphragm walls and ensure a safe excavation.

- (3) Further investigation through physical model experiments and numerical simulation analysis is required to uncover the mechanism of how karst caves affect the performance of diaphragm walls. Despite its limitations, the findings of this study can offer valuable insights for the design and construction of deep excavations.

## Data Availability

The data used to support the findings of this study are available from the corresponding author upon request.

## Conflicts of Interest

The authors declare that there are no conflicts of interest regarding the publication of this paper.

## Acknowledgments

This research was substantially supported by Guangzhou Metro Design & Research Institute Co., Ltd., Guangzhou, China.

## References

- [1] G. Zheng, C.-F. Zeng, Y. Diao, and X.-L. Xue, "Test and numerical research on wall deflections induced by pre-excavation dewatering," *Computers and Geotechnics*, vol. 62, pp. 244–256, 2014.
- [2] Y. Tan, D. Wang, Y. Lu, and T. Fang, "Excavation of middle Huai-hai road station of Shanghai metro line13: challenges, risks, countermeasures, and performance assessment," *Practice Periodical on Structural Design and Construction*, vol. 22, no. 3, Article ID 05017003, 2017.

- [3] K. Elbaz, S.-L. Shen, Y. Tan, and W.-C. Cheng, "Investigation into performance of deep excavation in sand covered karst: a case report," *Soils and Foundations*, vol. 58, no. 4, pp. 1042–1058, 2018.
- [4] C. Guo, J. Ye, C. Zhao, and F. Wang, "Mechanical and deformation characteristics of composite assembled supporting structure," *Geotechnical Research*, vol. 7, no. 4, pp. 230–243, 2020.
- [5] C. Guo, R. Wang, P. Lin, and F. Wang, "Numerical analyses of a prefabricated retaining system for foundation pits in silt soils," *Geotechnical Research*, vol. 7, no. 3, pp. 173–190, 2020.
- [6] Y. Tan, Y. Lu, C. Xu, and D. Wang, "Investigation on performance of a large circular pit-in-pit excavation in clay-gravel-cobble mixed strata," *Tunnelling and Underground Space Technology*, vol. 79, no. 1, pp. 356–374, 2018.
- [7] Y. Pan, H. Fang, B. Li, and F. Wang, "Stability analysis and full-scale test of a new recyclable supporting structure for underground eco-logical granaries," *Engineering Structures*, vol. 192, no. 1, pp. 205–219, 2019.
- [8] Y. Tan, B. Wei, X. Zhou, and Y. Diao, "Lessons learned from construction of Shanghai metro stations: importance of quick excavation, prompt propping, timely casting, and segmented construction," *Journal of Performance of Constructed Facilities*, vol. 29, no. 4, Article ID 04014096, 2015.
- [9] S. Liu, J. Yang, J. Fu, and X. Zheng, "Performance of a deep excavation irregular supporting structure subjected to asymmetric loading," *International Journal of Geomechanics*, vol. 19, no. 7, Article ID 05019007, 2019.
- [10] G. W. Clough, E. M. Smith, and B. P. Sweeney, "Movement control of excavation support systems by iterative design," in *Proceedings of Foundation Engineering: Current Principles and Practices*, pp. 869–884, New York, USA, 1989.
- [11] H. J. Liao and C. C. Lin, "Case studies on bermed excavation in Taipei silty soil," *Canadian Geotechnical Journal*, vol. 46, no. 8, pp. 889–902, 2009.
- [12] D. Li, Z. Li, and D. Tang, "Three-dimensional effects on deformation of deep excavations," *Proceedings of the Institution of Civil Engineering—Geotechnical Engineering*, vol. 168, no. 6, pp. 551–562, 2015.
- [13] R. Ignat, S. Baker, S. Liedberg, and S. Larsson, "Behavior of braced excavation supported by panels of deep mixing columns," *Canadian Geotechnical Journal*, vol. 53, no. 10, pp. 1671–1687, 2016.
- [14] H.-M. Lyu, S.-L. Shen, Y.-X. Wu, and A.-N. Zhou, "Calculation of groundwater head distribution with a close barrier during excavation dewatering in confined aquifer," *Geoscience Frontiers*, vol. 12, no. 2, pp. 791–803, 2021.
- [15] Y. H. Zhu, F. X. Sun, M. Q. Liu, Q. F. Liu, X. C. Li, and G. Ge, "Numerical simulation study on construction effect of top-down construction method of suspended diaphragm wall for deep and large foundation pit in complex stratum," *Advances in Civil Engineering*, vol. 2022, Article ID 8201726, 20 pages, 2022.
- [16] T. Yang, S. Xiong, S. Liu, Y. Liu, H. Zhao, and Y. Li, "Numerical analysis of the influence of deep foundation pit construction on adjacent subway stations in soft soil areas," *Advances in Civil Engineering*, vol. 2022, Article ID 6071868, 14 pages, 2022.
- [17] Y. Quan, X. Tan, Z. G. Hu, and M. H. Huang, "Measurement and analysis of deformation of underlying tunnel induced by foundation pit excavation," *Advances in Civil Engineering*, vol. 2023, Article ID 8897139, 12 pages, 2023.
- [18] W. Zhong, N. Huang, N. Nie, H. Ding, and F. Gao, "Study on the influence of excavation of superlarge and ultra-deep foundation pits on the pile foundation of existing viaducts," *Advances in Civil Engineering*, vol. 2023, Article ID 5834958, 13 pages, 2023.
- [19] J. P. Hsi and J. C. Small, "Ground settlements and drawdown of the water table around an excavation," *Canadian Geotechnical Journal*, vol. 29, no. 5, pp. 740–756, 1992.
- [20] C.-Y. Ou, P.-G. Hsieh, and D.-C. Chiou, "Characteristics of ground surface settlement during excavation," *Canadian Geotechnical Journal*, vol. 30, no. 5, pp. 758–767, 1993.
- [21] Y. Tan, D. Fan, and Y. Lu, "Statistical analyses on a database of deep excavations in Shanghai soft clays in China from 1995–2018," *Practice Periodical on Structural Design and Construction*, vol. 27, no. 1, Article ID 04021067, 2022.
- [22] G. W. Clough and T. D. O'Rourke, "Construction induced movements of in situ walls," *Specialty Conference on Design and Performance of Earth Retaining Structure*, no. 25, pp. 439–470, 1990.
- [23] J. H. Wang, Z. H. Xu, and W. D. Wang, "Wall and ground movements due to deep excavations in Shanghai soft soils," *Journal of Geotechnical and Geoenvironmental Engineering*, vol. 136, no. 7, pp. 985–994, 2010.
- [24] S.-S. Lin, N. Zhang, A. Zhou, and S.-L. Shen, "Risk evaluation of excavation based on fuzzy decision-making model," *Automation in Construction*, vol. 136, Article ID 104143, 2022.
- [25] R. A. Abdelrahman, A. M. Hassan, and M. I. Amer, "3D finite element analysis of diaphragm wall construction stages in sand," *Soils and Rocks*, vol. 42, no. 3, pp. 311–322, 2019.
- [26] W. Teparaksa and J. Teparaksa, "Comparison of diaphragm wall movement prediction and field performance for different construction techniques," *Underground Space*, vol. 4, no. 3, pp. 225–234, 2019.
- [27] A. James and B. Kurian, "Design specifications for diaphragm wall: state of the art," *Indian Geotechnical Journal*, vol. 50, no. 5, pp. 838–847, 2020.
- [28] H.-J. Zhao, W. Liu, P.-X. Shi, J.-T. Du, and X.-M. Chen, "Spatiotemporal deep learning approach on estimation of diaphragm wall deformation induced by excavation," *Acta Geotechnica*, vol. 16, no. 11, pp. 3631–3645, 2021.
- [29] R. Zhang, C. Wu, A. T. C. Goh, T. Böhlke, and W. Zhang, "Estimation of diaphragm wall deflections for deep braced excavation in anisotropic clays using ensemble learning," *Geoscience Frontiers*, vol. 12, no. 1, pp. 365–373, 2021.
- [30] Q. Ou, L. Zhang, M. Zhao, and Y. Wang, "Lateral displacement and internal force in diaphragm walls based on principle of minimum potential energy," *International Journal of Geomechanics*, vol. 19, no. 6, Article ID 04019055, 2019.
- [31] M. Kawa, W. Puła, and A. Truty, "Probabilistic analysis of the diaphragm wall using the hardening soil-small (HSs) model," *Engineering Structures*, vol. 232, no. 2021, Article ID 111869, 2021.
- [32] Y. Shao, C. Chen, Z. Lu, Y. Zheng, and Y. Zhang, "An intelligent leakage detection method for diaphragm wall joints based on fiber Bragg grating sensors and intelligent algorithms," *Measurement*, vol. 197, no. 2022, Article ID 111339, 2022.
- [33] G. Zheng, Q. H. Li, X. S. Cheng et al., "Diaphragm wall deformation and ground settlement caused by dewatering before excavation in strata with leaky aquifers," *Géotechnique*, vol. 74, no. 1, 2022.
- [34] R. Wang, S. Liu, L. Xu, C. Zhao, P. Ni, and W. Zheng, "Performance of a 56 m deep circular excavation supported by diaphragm and cut-off double-wall system in Shanghai soft ground," *Canadian Geotechnical Journal*, vol. 60, no. 4, pp. 521–540, 2023.